



Simulation of damage and failure processes of interpenetrating SiC/Al composites subjected to dynamic compressive loading

Guoju Li, Xu Zhang, Qunbo Fan*, Linlin Wang, Hongmei Zhang, Fuchi Wang, Yangwei Wang

National Key Laboratory of Science and Technology on Materials under Shock and Impact, School of Materials Science and Engineering, Beijing Institute of Technology, Beijing 100081, China

Received 26 March 2014; received in revised form 6 June 2014; accepted 18 June 2014
Available online 19 July 2014

Abstract

In the current study, a 3-D microscopic structural finite element (FE) model of interpenetrating SiC/Al composites (SiC/Al IPCs) is built, based on X-ray tomography and optimized methods for 3-D mesh generation. In addition, an interface model is introduced into the 3-D FE model to investigate the effects of the interfaces on the damage and failure processes, which includes a “tie-break contact” method at the SiC/Al interfaces. Subsequently, FE methods are applied to investigate the dynamic compression response of the 3-D FE model. To validate the numerical simulation results, the dynamic compression responses of SiC/Al IPCs are measured at strain rates of 2000 s^{-1} using a split Hopkinson pressure bar device. Our results show that failure of the SiC phase occurs just before the effective stress reaches its peak, but it plays a leading role in bearing the pre-metaphase stage of the load. From the point of energy dissipation, however, the contribution of Al phase cannot be ignored in the final stage of failure because the residual Al phase absorbs 30% of the energy of the global model by plastic deformation, even though its mass failure ratio is only 2%. Further microanalysis shows that the cracks initiate and propagate mainly near the SiC/Al interface, just on the side of the SiC ceramic phase. As the cracks extend further into the SiC phase, there appears a new “interface debonding” failure mode. These results show that brittle fracture of the SiC ceramic phase plays a key role in crack initiation, since the presence of complex 3-D SiC/Al interfaces usually causes the generated cracks to deflect before interconnecting with each other. This significantly retards propagation of the cracks, and thus increases the ductility of the composite materials. In the final stage of failure, the cracks are interconnected with each other in the SiC phase while the Al phase still maintains a degree of structural integrity. It is found that there exists obvious plastic deformation in local, relatively narrow, regions in the Al phase, and the local necking and tearing fractures tend to be localized in these severely deformed regions. Numerical simulation results are consistent with the observed behavior.

© 2014 Acta Materialia Inc. Published by Elsevier Ltd. All rights reserved.

Keywords: SiC/Al IPCs; 3-D microscopic structure FE model; Interface model; Dynamic damage and failure process

1. Introduction

Unlike traditional discrete-phase reinforced composites, interpenetrating composites (IPCs) are composed of two or more continuous phases. Each phase forms a completely

interconnected network [1–5]. Such a special structure endows the composite with a unique set of properties, since the strength, hardness, fracture toughness and other physical and mechanical properties can be tailored by adjusting the volume fraction of each phase and the interpenetrating phase morphology. One important observation is that the contribution of each phase’s desirable properties is expected to be maximized as a whole [6]. A number of novel IPCs have been developed. The primary uses for

* Corresponding author. Tel.: +86 10 68911144 863; fax: +86 10 68911144 866.

E-mail address: fanqunbo@bit.edu.cn (Q. Fan).

these composites are in the aerospace industry [7], the automotive industry [8,9] and, more recently, for the military community [10,11].

Due to its importance in engineering applications and for a theoretical understanding of IPCs, considerable attention has been directed toward their micromechanical behavior and failure mechanisms. Zhou et al. [2] fabricated an interpenetrating Al_2O_3 -TiC/Al composite, and investigated its fracture characteristics by in situ scanning electron microscopy (SEM) observations. It was found that the pure Al-based IPCs followed plastic deformation behavior, while the 2024Al-based IPCs presented a brittle fracture behavior. Hence, the metal–matrix chemistry played an important role in deciding the fracture behavior of the composites. Gao et al. [12] studied the fracture behavior of interpenetrating NiAl/TiC composites. In this case, the fracture surface showed that the combination of the debonding of TiC and NiAl interfaces and the cleavage of TiC grains was the main fracture mode of the composites. By keeping the volume fractions of the constituent phases constant, Vaucher et al. [13] examined the effects of the cell size of the ceramic foam on the ultimate tensile strength and the elongation tolerance of the interpenetrating SiOC–Al composites. It was found that the relatively small cell size improved the mechanical properties of the composite, due to the larger interface area.

Until now, however, it has been almost impossible to track the dynamic fracture process using conventional experimental methods, thus making it extremely difficult to reveal the underlying fracture mechanism of IPCs. Fortunately, numerical simulation methods seem to be able to avoid such a limitation. For example, using finite element (FE) methods based on artificial array geometrical models, the elastic modulus, yield strength and the coefficient of thermal expansion can be simulated [14,15]. Recently, a more realistic approach resorted to 3-D microtomography to represent the 3-D structure of IPCs. In this way, the thermal stresses and damage in Cu/ Al_2O_3 could be predicted numerically [16]. Nevertheless, as pointed out by Basista and Weglewski [17], modeling of fracture and crack growth of IPCs is still in its infancy. There are still only a few fracture models for interpenetrating composites that account for real spatial distributions of the constituent phases. Leon and Mishnaevsky [18] employed the representative volume element (RVE) model, based on the digital image-based modeling technique, together with voxel array-based methods of 3-D mesh generation, to simulate the deformation and damage evolution of the IPC. Though such a model was able to reflect the real structure compared with the idealized unit cell model, it ignored the weak-interface effects in the composites, which inevitably brought into question the validity of the calculation.

By employing X-ray tomography and FE technologies, the dynamic damage and failure process of interpenetrating SiC/Al composites (SiC/Al IPCs), subjected to compression loadings under high strain rate, is investigated in this

work. SiC is selected as a three-dimensionally continuous reinforcing phase, due to its low density, high compressive strength and high hardness, coupled with metallic Al as a continuous binder to improve the toughness. In addition, a “tie-break contact” model at the SiC/Al IPCs interfaces is taken into account, in order to investigate the effects of the interfaces on the damage and failure processes.

2. Experimental and computational approaches

2.1. Material preparation and dynamic compression experiment

The SiC/Al IPCs used in this study were prepared by vacuum-pressure infiltration technology. A volume fraction of 20% A356 aluminum casting alloy was used as the infiltrant. The cells of the precursor SiC foams had an average diameter of 20 μm . Cylindrical samples of 6 mm diameter and 6 mm length were shaped from the composite ingot to conduct the dynamic compression experiment. In the study, the uniaxial dynamic compression experiments were carried out with a split-Hopkinson pressure bar (SHPB) device. As shown in Fig. 1, the SHPB device consisted of a launcher device, a striker (14.5 mm diameter and 200 mm long), a pulse shaper, an incident bar (14.5 mm diameter and 1200 mm long), a transmitter bar (14.5 mm diameter and 1200 mm long), an absorbing bar (14.5 mm diameter and 1200 mm long), two strain gages (one on each of the middle of incident and transmitter bars), two jacked platens (one on each of the end surfaces of the incident and transmitter bars), an ultradynamic strain gage and an electronic data processing system. The sample, the end surfaces of which were coated with a thin layer of petroleum jelly to minimize friction at the interfaces between the sample and the two bars, was held snugly between the incident and the transmitter bars before loading. Both the striker and the bars were made of maraging steel of the same diameter in order to eliminate any impedance mismatch between them. The jacketed platens, made of tungsten which was jacketed by high-strength steel sleeves with the shrink-fit carbide technique, were inserted between the specimen and the bars to protect the bars' end surfaces. The pulse shaper, a 4.0 mm diameter disk made of copper, was used at the front end of the incident bar to ensure the equilibrium of the stresses in the specimen simultaneously. In this study, the average strain rate was 2000 s^{-1} .

2.2. X-ray tomography and 3-D reconstruction

A SiC/Al cube sample ($3 \times 3 \times 3 \text{ mm}^3$) was scanned using a Sky-Scan 1172 microcomputer tomography (micro-CT) scanner [19]. Images were obtained at 50 kV and 800 μA , which correspond to a resolution of 2.2 μm , with a 0.7° rotation step and a 0.5 mm aluminum filter. Subsequently, the transmission X-ray images were then reconstructed into high-resolution tomographic images

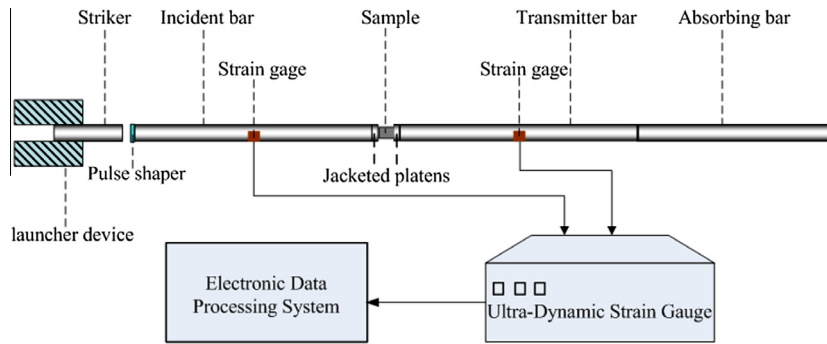


Fig. 1. Schematic of the SHPB device.

(voxel size $2.2 \times 2.2 \times 2.2 \mu\text{m}^3$) using Sky-Scan's cluster reconstruction software (NRecon). The Simpleware commercial package [20] was used to reconstruct the 3-D model from the high-resolution tomographic images. These tomographic images were segmented, smoothed and then reconstructed to a variety of 3-D microscopic models by the Simpleware's Scan IP module, which offers an extensive selection of image processing tools to assist the user in visualizing and segmenting regions of interest from any volumetric 3-D data (e.g. magnetic resonance imaging, CT, micro-CT). Fig. 2 shows the generated 3-D FE model ($0.5 \times 0.5 \times 0.5 \text{ mm}^3$) of the SiC/Al composite, as well as the SiC skeleton and Al. Subsequently, these models were imported to the ScanFE module, which provides a robust approach for converting segmented 3-D image data into a volumetric mesh. By using the marching-cubes algorithm, which should always attempt to group clusters of tetrahedra to form hexahedra wherever possible, 3-D FE models with mixed tetrahedral/hexahedral meshes were generated. In addition, 20 iterations of the anti-aliasing algorithm and two iterations of Laplacian smoothing were also employed to make the interfaces between the SiC skeleton and the Al smooth. Furthermore, by applying the interior mesh adaptation technique, the mesh density at the surfaces was preserved whilst being reduced elsewhere. Fig. 3 shows the built 3-D FE model ($0.5 \times 0.5 \times 0.5 \text{ mm}^3$) containing 323,908 tetrahedral elements and 80,977 hexahedral ones. These 3-D FE models were then exported to the Ansys/LS-DYNA software for numerical analysis.

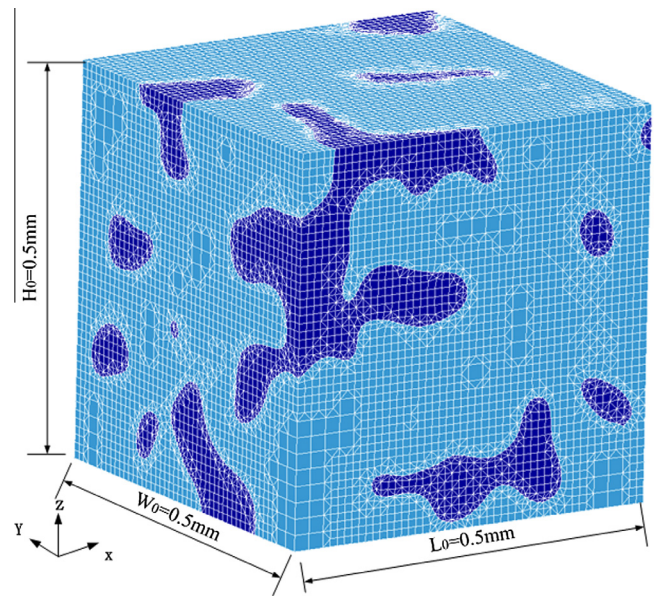


Fig. 3. 3-D FE model of SiC/Al IPCs.

2.3. Material properties

Johnson–Holmquist and Johnson–Cook constitutive models [21,22] were used to describe the SiC ceramic phase and Al metallic phase, respectively. Generally, the Johnson–Holmquist constitutive model is used for modeling brittle materials such as ceramics and glass. Of particular

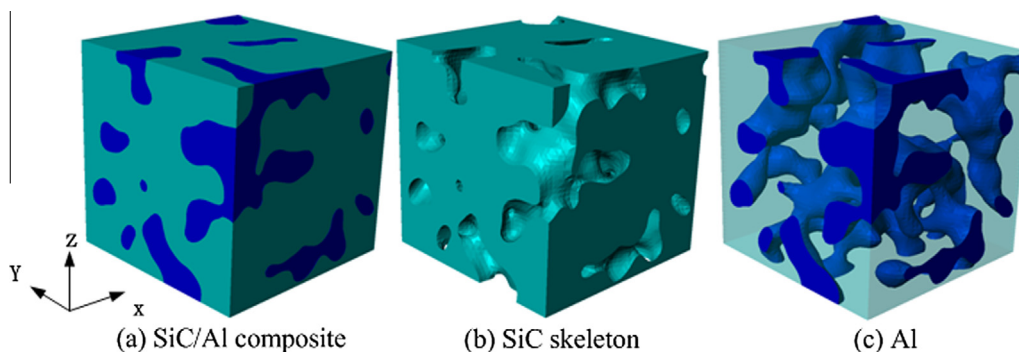


Fig. 2. 3-D reconstruction of SiC/Al IPCs.

note is that the strength and pressure are normalized by dividing by the pressure component of the Hugoniot elastic limit. The normalized equivalent stress is given by Eqs. 1–3:

$$\sigma^* = \sigma_i^* - D_{\text{JH2}}(\sigma_i^* - \sigma_f^*) \Big|_{0 < D_{\text{JH2}} < 1_{(\text{damaged})}} \quad (1)$$

$$\sigma_i^* = A_{\text{JH2}}(P^* + T_{\text{JH2}}^*)^{n_{\text{JH2}}} (1 + c_{\text{JH2}} \ln \dot{\epsilon}_{\text{JH2}}^*) \Big|_{D_{\text{JH2}}=0_{(\text{int act})}} \quad (2)$$

$$\sigma_f^* = \min \left[B_{\text{JH2}} P^{*m} (1 + c_{\text{JH2}} \ln \dot{\epsilon}_{\text{JH2}}^*) \Big|_{D_{\text{JH2}}=1_{(\text{fractured})}}, \text{SFMX} \right] \quad (3)$$

where σ_i^* is the normalized intact equivalent stress, σ_f^* is the normalized fracture equivalent stress, $\dot{\epsilon}_{\text{JH2}}^*$ is the normalized strain rate (see Eq. (4)), P^* is the normalized pressure (see Eq. (5)), T_{JH2}^* is the normalized maximum tensile hydrostatic pressure (see Eq. (6)), SFMX is the normalized fracture strength, A_{JH2} , B_{JH2} , c_{JH2} , n_{JH2} and m_{JH2} are material constants and D_{JH2} (see Eq. (7)) are the damage parameters.

$$P^* = \frac{P}{P_{\text{HEL}}} \quad (4)$$

$$T_{\text{JH2}}^* = \frac{T_{\text{max}}}{P_{\text{HEL}}} \quad (5)$$

$$\dot{\epsilon}_{\text{JH2}}^* = \frac{\dot{\epsilon}}{\dot{\epsilon}_0} \quad (6)$$

$$D_{\text{JH2}} = \sum \frac{\Delta \bar{\epsilon}^p}{\epsilon_f^p} \quad (7)$$

Here, P is the hydrostatic pressure, P_{HEL} is the pressure component of the Hugoniot elastic limit, T_{max} is the maximum tension hydrostatic pressure, $\dot{\epsilon}$ is the strain rate, $\dot{\epsilon}_0$ is the reference strain rate, $\Delta \bar{\epsilon}^p$ (see Eq. (8)) is the plastic strain during a cycle of integration and ϵ_f^p is the plastic strain to fracture under a constant pressure P .

$$\epsilon_f^p = D_{\text{JH2}-1} (P^* + T_{\text{JH2}}^*)^{D_{\text{JH2}}-2} \quad (8)$$

where $D_{\text{JH2}-1}$ and $D_{\text{JH2}-2}$ are material constants.

The Johnson–Holmquist model parameters of SiC used in the study are listed in Table 1.

Correspondingly, the Johnson–Cook constitutive model, which is widely used in numerical models involving high strain rates and temperatures for metallic materials, was employed to model the Al metallic phase. In this model, the flow stress is described as Eq. (9):

$$\sigma_y = (A + B \bar{\epsilon}^n) (1 + c \ln \dot{\epsilon}^*) (1 - T^{*m}) \quad (9)$$

where A , B , n , c and m are the material constants, $\bar{\epsilon}^p$ is effective plastic strain, $\dot{\epsilon}^*$ (see Eq. (10)) is the normalized effective total strain rate and T^* (see Eq. (11)) is the homologous temperature.

$$\dot{\epsilon}^* = \frac{\dot{\epsilon}}{\dot{\epsilon}_0} \quad (10)$$

$$T^* = \frac{T - T_{\text{room}}}{T_{\text{melt}} - T_{\text{room}}} \quad (11)$$

where $\dot{\epsilon}$ is the effective total strain rate, $\dot{\epsilon}_0$ is the effective reference strain rate, T is the temperature, T_{room} is the reference temperature, T_{melt} is the melting temperature.

In addition, the strain at fracture is given by Eq. (12):

$$\epsilon^f = (D_1 + D_2 \exp D_3 \sigma^*) (1 + D_4 \ln \dot{\epsilon}^*) (1 + D_5 T^*) \quad (12)$$

where D_1 , D_2 , D_3 , D_4 and D_5 are the material constants and σ^* is the ratio of pressure divided by effective stress.

Fracture occurs when the damage parameter D (see Eq. (13)) reaches the value of 1:

$$D = \sum \frac{\Delta \bar{\epsilon}^p}{\epsilon^f} \quad (13)$$

where $\Delta \bar{\epsilon}^p$ is the plastic strain during a cycle of integration.

The Johnson–Cook model parameters of Al used in the study are listed in Table 2.

2.4. Boundary and loading conditions

The model was subjected to uniaxial dynamic compression by defining a moving rigid wall on one of its own six sides as well as a fixed rigid wall on the opposite side. The loading curve of the moving rigid wall was defined as follows: the velocity in the compression direction was increased linearly from 0 to the peak velocity (V_{peak}), which is given by Eq. (14) to within 0.2 μs , then kept constant until $t = 9.8 \mu\text{s}$ to ensure a constant strain rate of 2000 s^{-1} , and finally decreased linearly to 0 at $t = 10 \mu\text{s}$. Considering the random space distribution characteristics of the IPC microstructure, the compression load is applied in the x , y and z directions, respectively. Fig. 4 illustrates the loading process in the z direction.

$$V_{\text{peak}} = \dot{\epsilon}_{\text{ave}} \times H_0 \quad (14)$$

where $\dot{\epsilon}_{\text{ave}}$ is the average strain rate and H_0 is the initial height of the model. In this investigation, $\dot{\epsilon} = 2000 \text{ s}^{-1}$ and $H_0 = 0.5 \text{ mm}$. Therefore, the peak velocity V_{peak} is 1 m s^{-1} .

In addition, the effective stress and strain of the model can be obtained from Eqs. (15) and (16):

$$\sigma_{\text{eff}} = |F|/A_0 \quad (15)$$

$$\epsilon_{\text{eff}} = \dot{\epsilon}_{\text{ave}} \times t \quad (16)$$

where F is the sum of the reaction forces at the nodes on the surface $Z = H$, A_0 is the initial area of that surface and t is the loading time.

Table 1
Johnson–Holmquist parameters of SiC.

A_{JH2}	n_{JH2}	c_{JH2}	B_{JH2}	m_{JH2}	T_{max} (GPa)	P_{HEL} (GPa)	SFMX	$D_{\text{JH2}-1}$	$D_{\text{JH2}-2}$
0.96	0.65	0	0.35	1.0	0.37	5.9	0.8	0.48	0.48

Table 2
Johnson–Cook model parameters of Al.

A (MPa)	B (MPa)	n	c	m	D_1	D_2	D_3	D_4	D_5
50	157	0.3	0.0083	1.7	0.112	0.123	−1.5	0.007	0

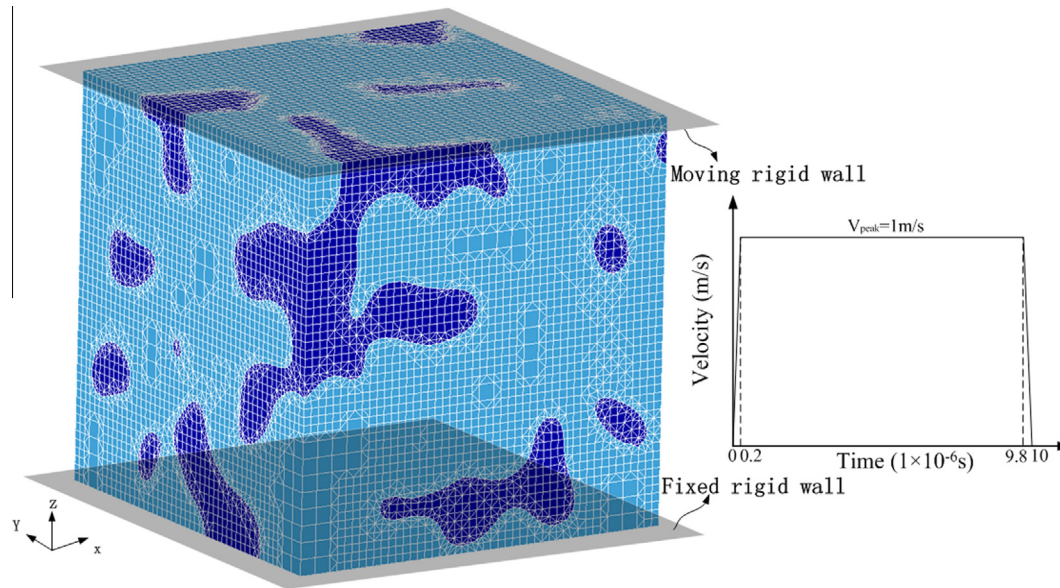


Fig. 4. The applied loading conditions of the 3-D FE model in the z direction.

2.5. Interface model

The interface of the SiC/Al IPCs is mainly composed of transition layer materials, including Al_2O_3 and Al_4C_3 . Compared with the dimensions of the SiC or Al phase, the thickness of the interface is very small, usually less than $0.2 \mu\text{m}$. In this case, the thickness of the interface can be ignored, and the “tie-break contact” model is employed to simulate the influence of the interface on the dynamic behavior of the SiC/Al IPCs. The “tie-break contact” model is defined by Eq. (17):

$$\left(\frac{|\sigma_n|}{\text{NFLS}}\right)^2 + \left(\frac{|\sigma_s|}{\text{SFLS}}\right)^2 \geq 1 \quad (17)$$

where σ_n and σ_s are the tension stress and the shear stress of the interface, respectively. NFLS and SFLS are the corresponding tension failure stress and shear failure stress, respectively. As shown in Fig. 5, the nodes at the SiC/Al interface are tied to each other before the tension stress and the shear stress of the interface meet the condition defined in Eq. (17); once the tension or shear stress failure criteria are satisfied, however, the tied nodes are separated from each other. In addition, the values for tension stress and shear stress of the interface were both given as 20 MPa, which was measured by using of the push-out test [23,24] in the study.

2.6. The details of FEM modeling used in LS-DYNA

In Ansys/LS-DYNA, the input data file is composed of a series of keywords, as illustrated in Fig. 6. It should be noted that the term “Part” is used, which combines the material information and element attributes for a set of specified elements. In the current study, the Part of SiC and the Part of Al were defined by pointing to the material card keywords *MAT_JOHNSON_HOLMQUIST_CERAMICS and *MAT_JOHNSON_COOK, respectively. In addition, the constant stress element identified by *SECTION_SOLID is used for both of the Parts. For the boundary and loading conditions, a moving rigid wall with a trapezoidal velocity–time curve defined by *RIGIDWLL_GEOMETRIC_FLAT_MOTION and *DEFINE_CURVE was applied on one of the six sides of the model, while *RIGIDWALL_PLANER was prescribed on the opposite side. For the interface model, the “tie-break contact” was implemented by using *CONTACT_AUTOMATIC_SURFACE_TO_SURFACE_TIEBREAK and *SET_SEGMENT, which incorporates the tension failure stress and shear failure stress to be defined. For parameters of solution control, the keywords *CONTROL_TERMINATION and *CONTROL_TIMESTEP were used to set the solution time and solution time step, respectively. Moreover, *CONTROL_HOURLGLASS is needed to avoid zero-energy deformation modes.

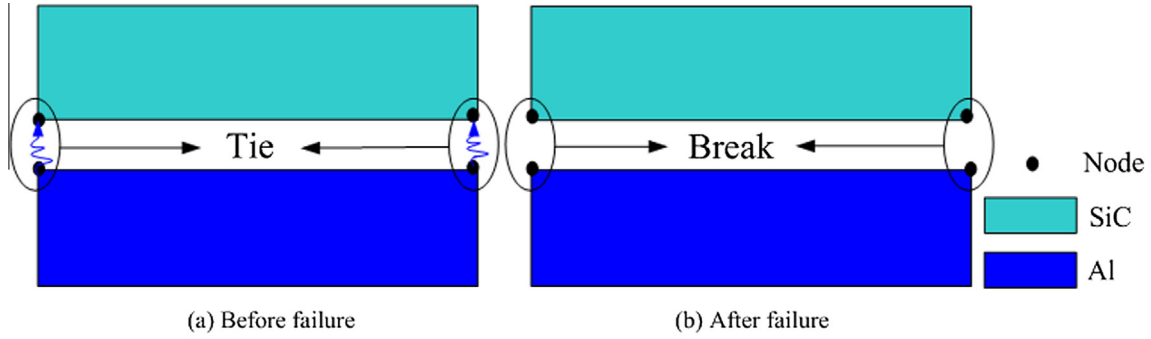


Fig. 5. Definition of the interface model.

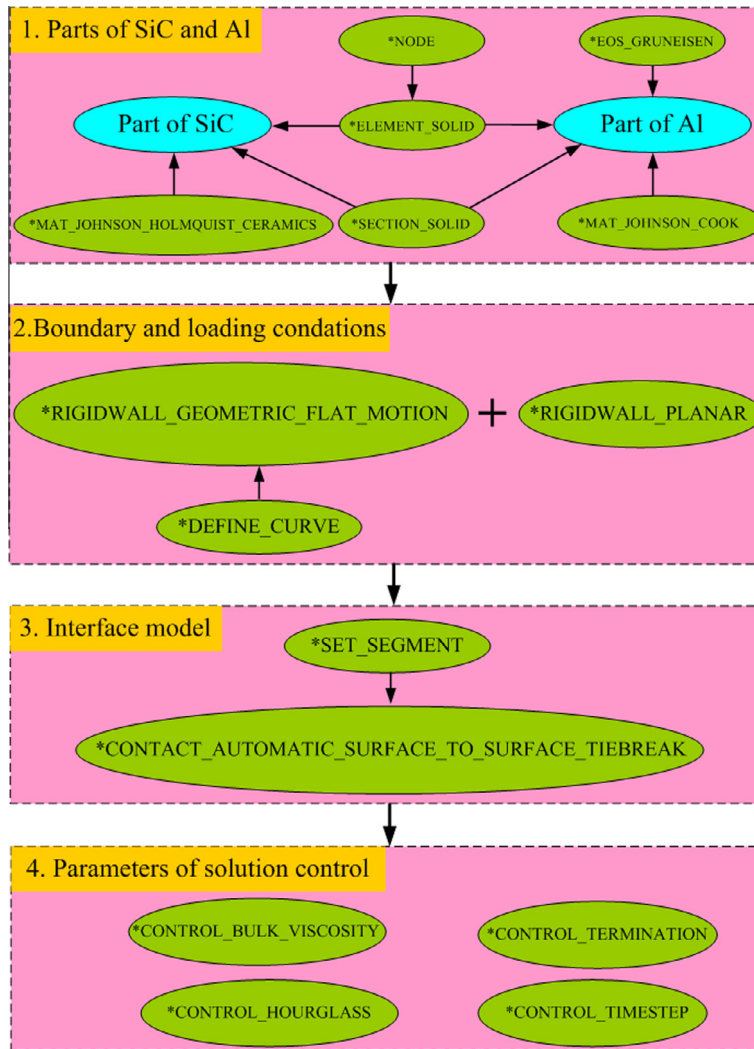


Fig. 6. The schematic diagram of the keywords used in Ansys/LS-DYNA.

3. Dynamic compression modeling

3.1. The macrodynamic damage and failure analysis

As shown in Fig. 7, the numerical simulation results of effective stress–strain curves under compression loads in the *x*, *y* and *z* directions (see Section 2.4) for the 3-D

SiC/Al IPCs model are compared with experimentally obtained results. It can be seen that the simulation results almost completely overlap the experimental results. To further investigate the effect of model size on the reliability of the numerical results, models with a series of different sizes were calculated and compared with the experimental results. Fig. 8 illustrates three representative models with

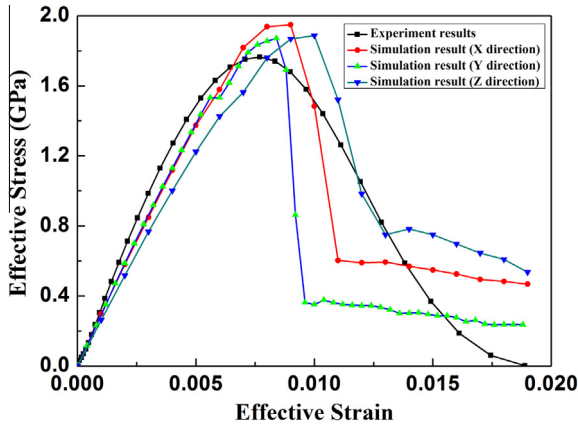


Fig. 7. The effective stress–strain curves of SiC/Al IPCs obtained from numerical and experimental results.

different sizes, i.e. $0.15 \times 0.15 \times 0.15 \text{ mm}^3$, $0.3 \times 0.3 \times 0.3 \text{ mm}^3$ and $0.5 \times 0.5 \times 0.5 \text{ mm}^3$. Considering the possible scattered results caused by the geometrical models and the intrinsic brittleness of the composites, a total of 30 models were randomly reconstructed for a specified size scale. Correspondingly, the distribution of the Al phase ratio for a specific sized model was obtained by the ScanIP module, as listed in Table 3. It can be seen that, by increasing the model size from $0.15 \times 0.15 \times 0.15 \text{ mm}^3$ to $0.5 \times 0.5 \times 0.5 \text{ mm}^3$, the variation range (the difference between the maximum and minimum Al phase ratio) of the Al phase ratio becomes narrower, from 7–38% to 19–22%, and gradually converges to a ratio of 20%, which reflects the realistic Al phase ratio of the SiC/Al IPCs, as mentioned in Section 2.1.

These models were subsequently imported into Ansys/LS-DYNA to calculate the effective stress–strain curves under virtual compression loads. As shown in Fig. 9, the shadow diagrams covering the calculated effective stress–strain curves with respect to different sized models are compared with the experimentally obtained results. It is evident

that the fluctuation range of the effective stress–strain curves of models attenuates rapidly with the increase in the size from $0.15 \times 0.15 \times 0.15 \text{ mm}^3$ to $0.5 \times 0.5 \times 0.5 \text{ mm}^3$, approaching the experimentally obtained curve. It should be mentioned, however, that the computation cost in terms of both time and memory requirements rise significantly with further increases in model size. Therefore, the 3-D FE model with the size of $0.5 \times 0.5 \times 0.5 \text{ mm}^3$ is acceptable. In conclusion, even though the dimensions of the 3-D FE model are only $0.5 \times 0.5 \times 0.5 \text{ mm}^3$, the phase ratio and space distribution of the 3-D FE model are reasonable and hence reflect the macromechanical properties of the SiC/Al IPCs.

In the FE analysis, the element is deleted once the given failure criteria for the material is satisfied, so the mass-loss ratio can be used as a measure of the degree of failure for the 3-D FE model for SiC/Al IPCs. The mass-loss ratio is defined by Eq. (18):

$$\eta = \frac{m_{failure}(t)}{m_{ini}} \quad (18)$$

where $m_{failure}(t)$ is the mass of the deleted elements of the SiC or Al phase as a function of time and m_{ini} is the initial mass of each phase.

Fig. 10 is the effective stress vs. time curve of the 3-D FE model for SiC/Al IPCs under a load in the z direction as well as the mass-loss ratio vs. time curves for the SiC and Al phases of the 3-D FE model. It can be seen that the effective stress increases very rapidly during the initial stage, reaching a peak value of 1.92 GPa at $t = 3.3 \mu\text{s}$, then

Table 3
Al phase ratio with different sizes of microscopic models.

Micromodel size (mm ³)	0.15 × 0.15 × 0.15	0.3 × 0.3 × 0.3	0.5 × 0.5 × 0.5
Al phase ratio (%)	7–38	15–29	19–22

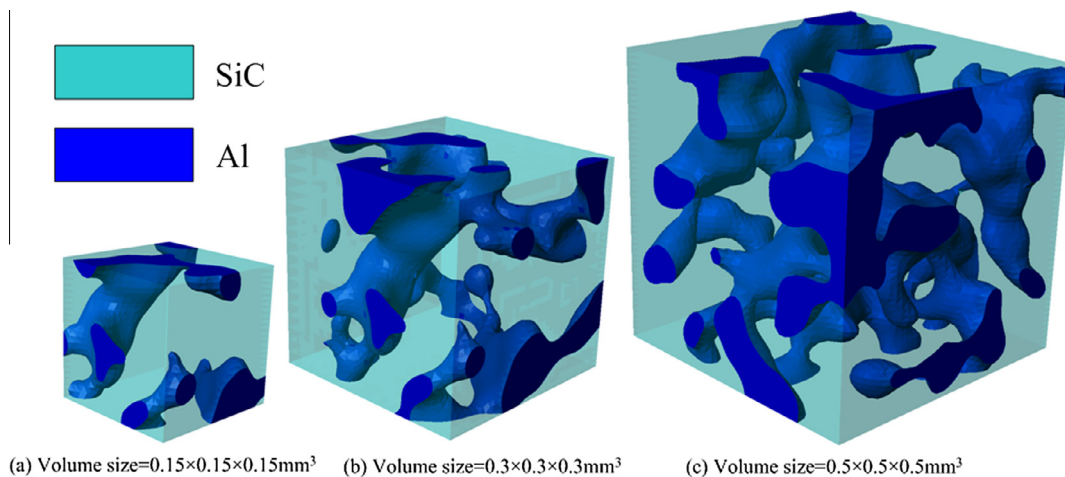


Fig. 8. Three representative models with different sizes.

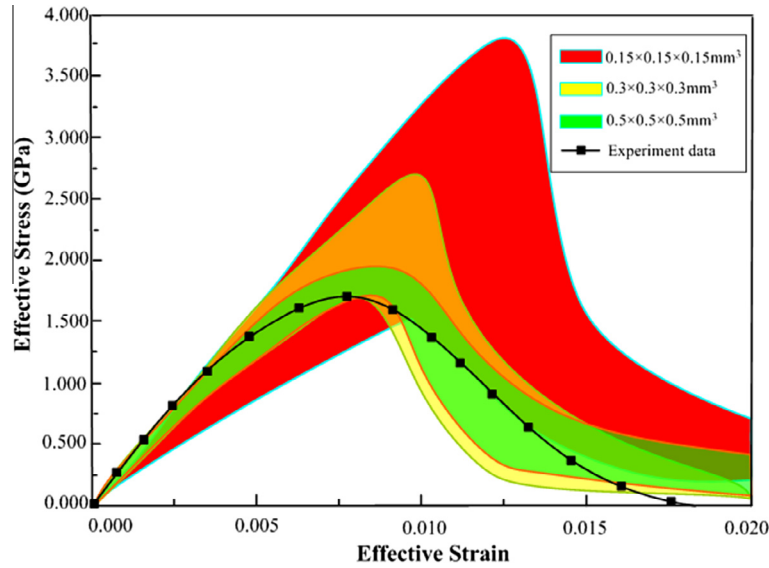


Fig. 9. The shadow diagrams covering the numerical simulation results of effective stress–strain curves under compression loads with different sizes for the 3-D SiC/Al IPCs model and the experimentally obtained results.

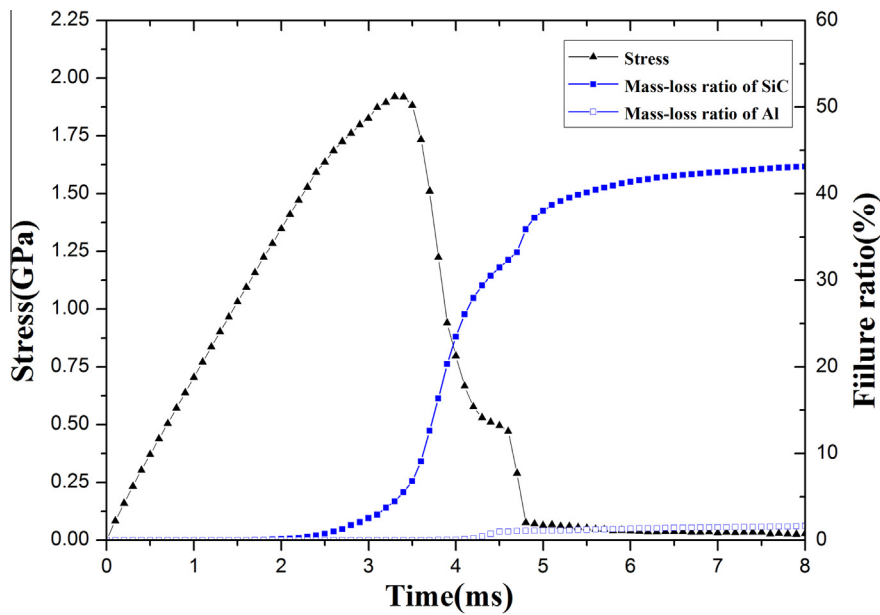


Fig. 10. Stress–time and mass evolution–time curves of the SiC and Al phases in the *z* direction.

drops significantly down to 0.578 GPa at $t = 4.2 \mu\text{s}$. Subsequently, the effective stress decreases slowly to 0.471 GPa at $t = 4.6 \mu\text{s}$, then drops immediately down to almost zero after $t = 4.8 \mu\text{s}$; this corresponds to the complete stress-collapse process of the 3-D FE model. It should be noted, however, that the failure process of the model occurs just before the effective stress begins to drop, which is reasonable if the mass-loss ratio curve is taken into account. In fact, the failure of the SiC phase appears at $t = 2.0 \mu\text{s}$ and the mass-loss ratio has increased to 5% when the time reaches $3.3 \mu\text{s}$, corresponding to the stress peak. Before the failure of the SiC phase occurs, the deformation behavior of the model is a linearly elastic deformation mode. Once

the failure of the SiC phase occurs, the model enters a non-linear strain-hardening stage, so the mass–loss ratio of the SiC phase increases rapidly to 37% from $3.3 \mu\text{s}$ to $4.6 \mu\text{s}$, accompanied by a rapid stress collapse of the model. At the final stage (from $4.6 \mu\text{s}$ to $8.0 \mu\text{s}$), the mass vs. loss ratio of the SiC phase remains almost constant, indicating that the failure of the SiC phase is almost complete. As shown in the mass-loss ratio vs. time curve of the Al phase, however, loss of the Al phase does not occur until many of the elements of the SiC phase are lost at $4.2 \mu\text{s}$. In fact, the mass-loss ratio of the Al phase peaks at only 2%, due to its good ductility. It is evident that the ceramic phase is the predominant contributor to damage of the model IPC.

In FE analysis, the internal energy of the FE model due to the elastic–plastic deformation of the elements can be recorded. Fig. 11 shows the internal energy vs. time curve results from the 3-D FE model, together with the individual SiC and Al phases. The internal energy given by the 3-D FE model is almost equal to that of SiC phase up to 3.3 μs . Evidently, the energy absorption by the whole model depends mainly on elastic deformation of the SiC phase over this period. After the internal energy of the 3-D FE model reaches its peak value, it decreases rapidly, since many SiC phase elements are deleted and hence the stored internal energy of the eroded elements is released. However, the internal energy of the 3-D FE model remains constant for the period 4.0–5.0 μs . Further analysis shows that, during this period, the internal energy of the SiC phase keeps on decreasing, while the internal energy of Al phase increases significantly, since the Al phase elements can accumulate more internal energy by severe plastic deformation. Beyond 4.7 μs , in the late stages of stress collapse, the internal energy of the residual Al phase is about 30% of the whole model. Obviously, the energy consumption of Al phase cannot be ignored, although the mass of the eroded Al phase is rather low.

3.2. The microdynamic damage and failure analysis

3.2.1. The process of crack initiation

Fig. 12 shows the failure contour of the SiC phase at $t = 2.0 \mu\text{s}$. In order to observe the cracks more intuitively, the failure elements of the SiC ceramic phase are explicitly displayed in the model. As shown in Fig. 12(a), several crack sources appear simultaneously in the region of the SiC phase, near the SiC/Al interface. For further study of the internal 3-D spatial distribution of the crack sources,

the non-failure elements of the SiC phase are deliberately hidden; only the Al phase and the failure elements of the SiC phase are displayed, and these are portrayed in different colors (see Fig. 12(b)). It is evident that all crack sources are initiated near the SiC/Al interface, but only on the side of the SiC ceramic phase. Fig. 13 shows the first principal stress contour of the model at $t = 0.9 \mu\text{s}$. It is found that the regions of stress concentration are located just where the crack sources appear, as illustrated in Fig. 12. Obviously, it is the local, relatively high, tensile stress that leads to the failure of the elements of the SiC phase, thus causing the initiation of multiple crack sources.

3.2.2. The process of crack propagation

Fig. 14(a) displays the evolution of the external damage of the model at $t = 3.6 \mu\text{s}$. Fig. 14(b) is taken from Fig. 14(a) to show the internal damage behavior. It can be seen very clearly that the cracks are further developed and distributed primarily inside the SiC ceramic phase, and the directions of most cracks are distributed along the loading direction.

With the further propagation of the cracks in the SiC phase, those initiated near the SiC/Al interfaces arrive at new SiC/Al interfaces. It is found that a new interface debonding failure mode appears, which is apparently different from the failure process inside the SiC phase. As shown in Fig. 15, multiple interface debonding phenomena appear in SiC/Al interfaces at $t = 4.0 \mu\text{s}$, labeled A, B, C and D. The interface between the SiC and Al phases begins to debond when the stress state in the interface satisfies the failure criteria defined in Section 2.5. Fig. 16 is a typical experimental SEM image, in which the interface debonding phenomenon can be clearly observed; it verifies the simulation results very well. For further study of the process of interface deb-

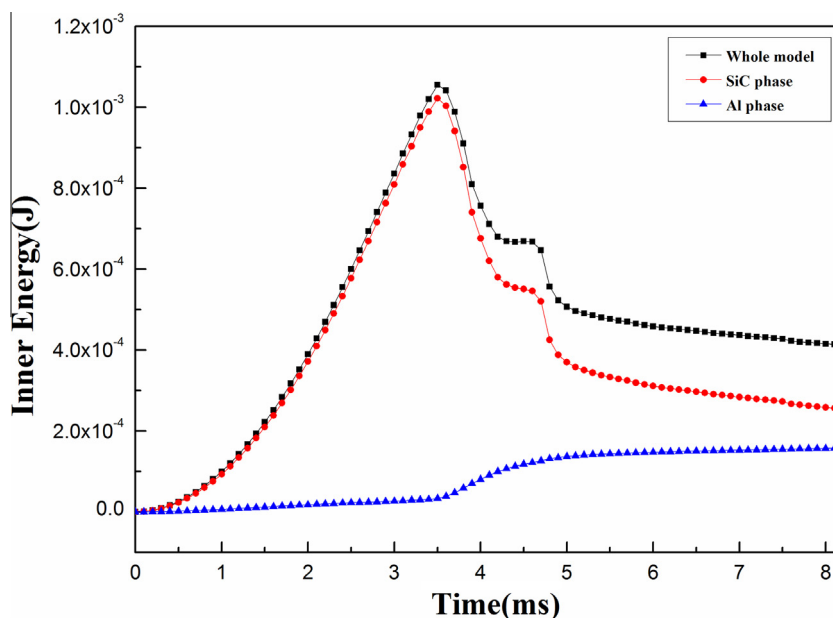


Fig. 11. The internal energy-time curves of the SiC/Al IPCs, together with individual SiC and Al phases.

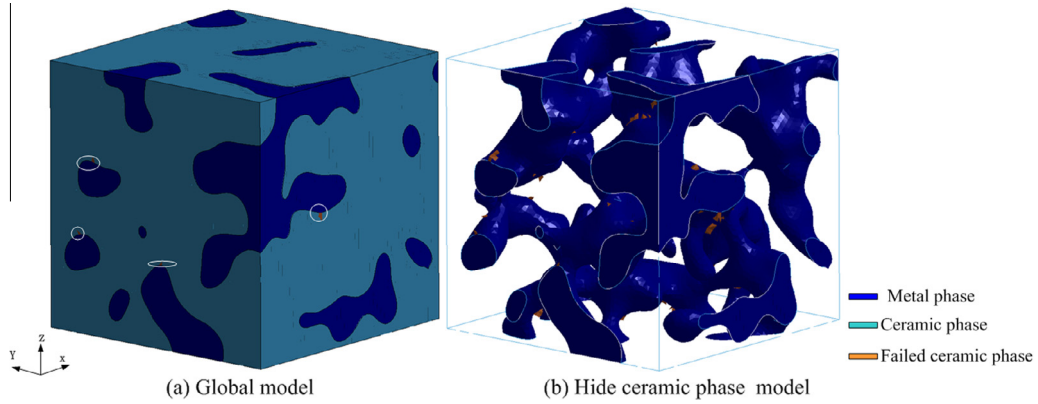


Fig. 12. The failure contour of the SiC phase at $t = 2.00 \mu\text{s}$.

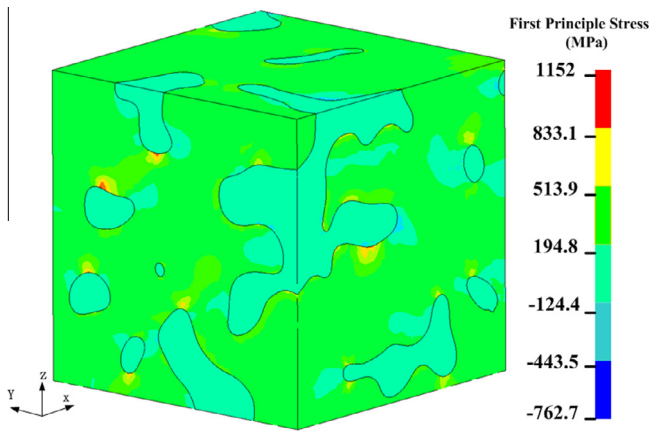


Fig. 13. The first principal stress contour of the 3-D FE model at $t = 0.9 \mu\text{s}$.

onding, the sequence from crack initiation, propagation and interface debonding in region A is traced and analyzed, with the results shown in Fig. 17. The crack initiation is generated both on the up and down sides of the SiC phase at $t = 2.4 \mu\text{s}$. Subsequently, the two cracks penetrate into the inner side of the SiC phase at $t = 3.2 \mu\text{s}$, thus making the interface bear a higher tension stress. As the two cracks develop further, their paths begin to deflect along the original interfaces at $t = 3.6 \mu\text{s}$, accompanied by the interface

debonding phenomenon. At $t = 4.0 \mu\text{s}$, the degree of interface debonding further increases until the two cracks are completely connected to each other. It can be seen that, although brittle fracture of the SiC ceramic phase plays a key role in crack initiation, the existence of complex 3-D SiC/Al interfaces usually causes the generated cracks to be deflected before connecting with each other. This significantly retards the propagation of the cracks and thus increases the ductility of the composite materials.

3.2.3. The final stage of failure

In the final stage of failure ($4.0\text{--}5.0 \mu\text{s}$), as shown in Fig. 18, there is an extensive region of collapse in the SiC phase, but the Al phase still retains a certain structural integrity. Fig. 19 shows the effective plain strain contours of the Al phase at different times. To observe the plastic deformation of the Al phase in 3-D space, the SiC phase is hidden. As shown in Fig. 19(a), there exists clear plastic deformation in the local, relatively narrow, regions in the Al phase at $t = 4.0 \mu\text{s}$. At $t = 5.0 \mu\text{s}$ (see Fig. 19(b)), local necking and tearing fractures tend to be localized in those severely deformed regions. This tearing phenomenon shown by Al can also be seen in the experimental dynamic compression results (see Fig. 20). Fig. 20 shows a typical SEM image of the tearing phenomenon in the Al phase,

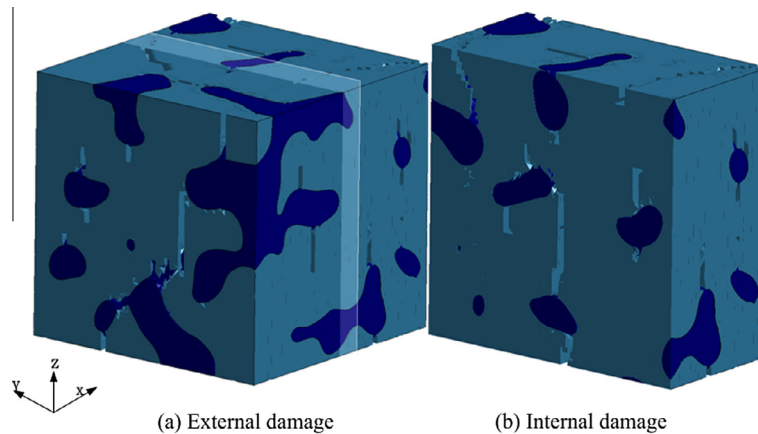


Fig. 14. Damage evolution of the 3-D FE model at $t = 3.6 \mu\text{s}$.

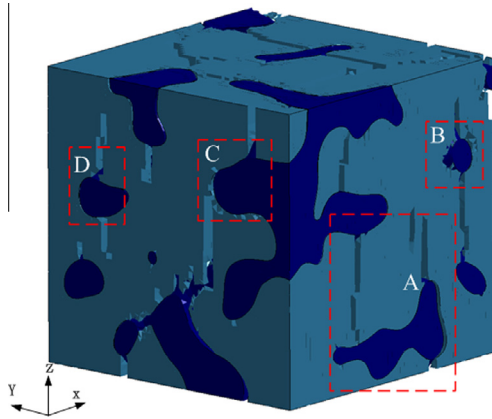


Fig. 15. The failure contour of the 3-D FE model at $t = 4.0 \mu\text{s}$ (multiple interface debonding phenomena appear in SiC/Al interfaces, labeled A, B, C and D).

which confirms the results of numerical simulation. As described in Section 3.1, the mass-loss ratio of the Al phase is only 2%, but the effect of energy dissipation of the residual Al phase, which maintains a certain degree of structural integrity in the late stage of failure, cannot be ignored.

4. Summary

In this investigation, a real 3-D microscopic structural FE model, reflecting the microstructural characteristics of SiC/Al IPCs, is established using X-ray tomography and FE technologies. In addition, a 2-D interface ignoring the thickness effect is employed successfully in this model by defining the “tie-break contact” between the Al and SiC phases. Subsequently, the model is applied to investigate the process of dynamic damage under axial compression

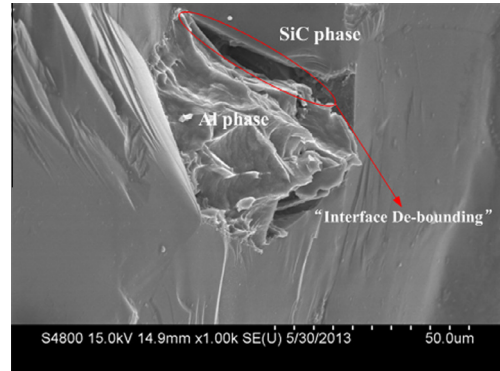


Fig. 16. Experimental SEM image of the SiC/Al IPCs showing the “interface debonding” phenomenon.

using FE techniques. The effective stress–strain curves obtained from simulation almost exactly match the experimental results, which indicates that this is a reasonably effective model for the macromechanical properties of SiC/Al IPCs. The curves of stress vs. time and mass evolution of the SiC and Al phases show that the failure process of the model occurs just before the effective stress begins to drop, at which point the SiC ceramic phase makes the dominant contribution to the pre-metaphase stage when failure of the model occurs. On the other hand, the contribution of the Al phase cannot be ignored in the final failure stage because the residual Al phase absorbs 30% of the energy of the global model by plastic deformation despite contributing only 2% of the mass failure ratio. From the microdynamic damage and failure analysis, it is found that the cracks initiate and propagate mainly near the SiC/Al interface, but only on the side of the SiC ceramic phase. The cracks develop further and are distributed primarily inside

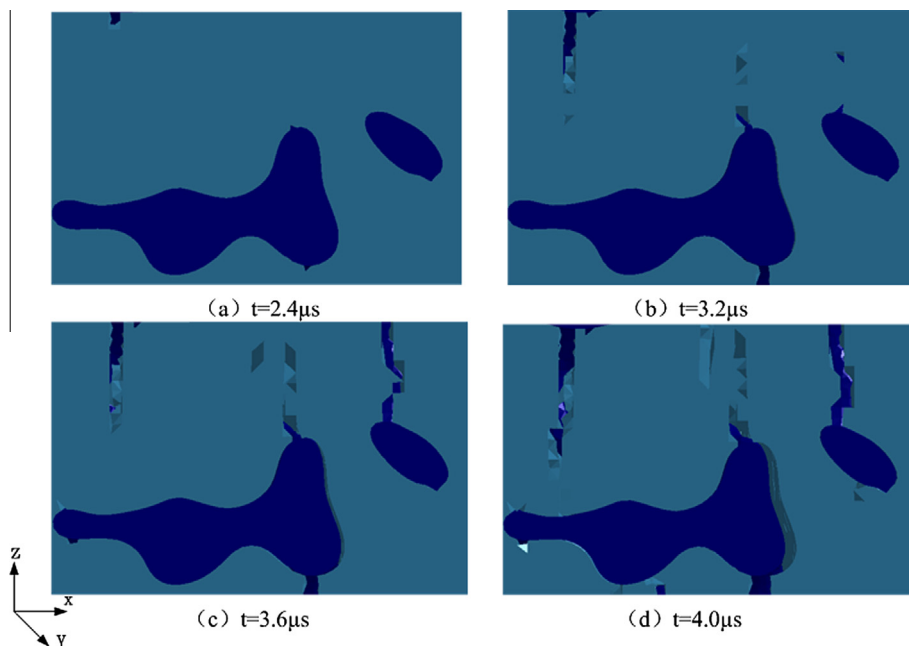


Fig. 17. The process from crack initiation and propagation to “interface debonding” in region A from.

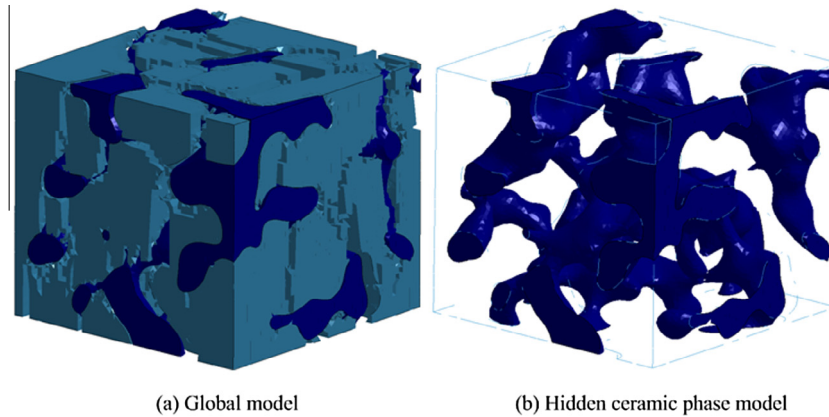


Fig. 18. The failure contours of the 3-D FE model at $t = 5.0 \mu\text{s}$.

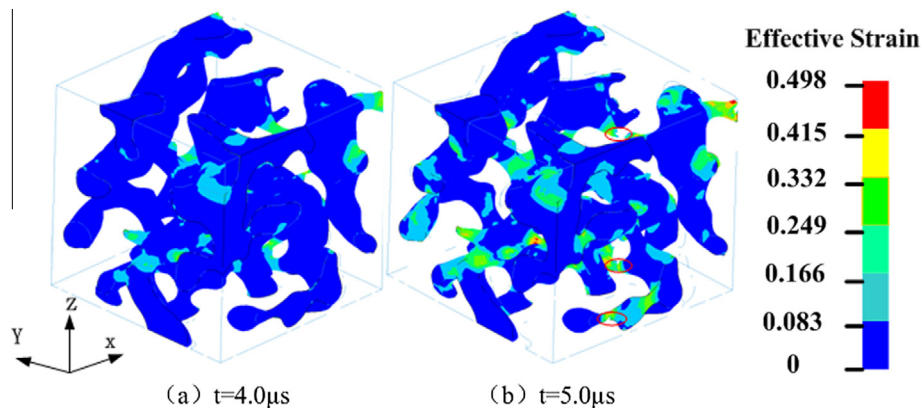


Fig. 19. The effective plain strain contours of Al at different times.

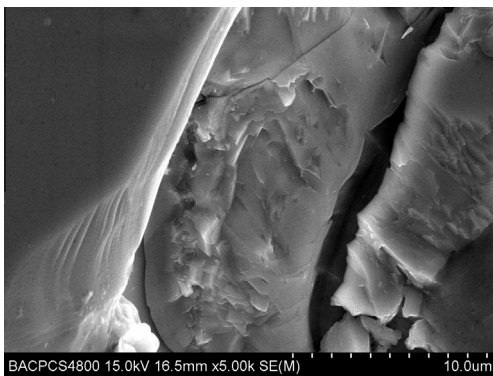


Fig. 20. Experimental SEM image of the tearing phenomenon in the Al phase.

the SiC ceramic phase, at which point a new “interface debonding” failure mode appears that is apparently different from the failure process inside the SiC phase. These results show that the presence of complex 3-D SiC/Al interfaces usually causes the generated cracks to be deflected before interconnecting with each other, which significantly retards the propagation of the cracks. This increases the ductility of the composite materials. In the final stage of failure, there is widespread collapse in the SiC phase, together with obvious plastic deformation in the local, relatively narrow,

regions in the Al phase. The numerical simulation results agree well with the experimental observations.

Acknowledgements

We gratefully acknowledge the financial support of the program for New Century Excellent Talents in University (NCET-12-0051).

References

- [1] Zhou W, Hu W, Zhang D. *Scr Mater* 1998;39(12):1743–8.
- [2] Zhou W, Hu W, Zhang D. *Mater Lett* 1999;40(4):156–60.
- [3] Horvitz D, Gotman I, Gutmanas EY, Gutmanas EG, Claussen N. *J Eur Ceram Soc* 2002;22(6):947–54.
- [4] Kim JS, Kwon YS, Lomovsky OL, Korchagin MA, Mail VL, Dudina DV. *Mater Lett* 2006;60:3723–6.
- [5] Chen Y, Wang A, Fu H, Zhu Z, Zhang H, Hu Z, et al. *Mater Sci Eng A* 2011;530:15–20.
- [6] Wegner LD, Gibson LG. *Int J Mech Sci* 2001;43(8):1771–91.
- [7] Han J, Hong H, Zhang X, Wang B. *Compos Sci Technol* 2005;65:1711–8.
- [8] Etter T, Kuebler J, Frey T, Schulz P, Löffler JF, Uggowitzer PJ. *Mater Sci Eng A* 2004;386:61–7.
- [9] Daehn GS, Breslin MC. *JOM* 2006;58(11):87–91.
- [10] Chang H, Binner J, Higginson R, Paul M, Peter W, Gus K. *Mater Sci Eng A* 2011;528(6):2239–45.

- [11] Periasamy C. A split hopkinson pressure bar apparatus for high strain rate testing of interpenetrating phase composites. Auburn University, 2010.
- [12] Gao M, Pan Y, Oliveira FG. *Mater Lett* 2004;58(11):1761–5.
- [13] Vaucher S, Kuebler J, Beffort O, Biasetto L, Zordan F, Colombo P. *Compos Sci Technol* 2008;68:3202–7.
- [14] Wegner LD, Gibson LJ. *Int J Mech Sci* 2000;42(5):925–42.
- [15] Feng X, Mai Y, Qin Q. In: Computational materials science twelfth international workshop on computational mechanics of materials, 2003.
- [16] Weglewski W, Basista M. Interpenetrating phase composites. In: European congress on computational methods in applied sciences and engineering, 2012.
- [17] Basista M, Weglewski WJ. *Theor Appl Mech Pol* 2006;44(3):455–84.
- [18] Leon L, Mishnaevsky J. *Mater Sci Eng A* 2005;407:11–23.
- [19] SkyScan NV, Aartselaar, Belgium. <<http://www.skyscan.be/>>.
- [20] Simpleware Ltd, Exeter, UK. <http://www.simpleware.com/>.
- [21] Liu G, Ni C, Xiao Q, Jin F, Qiao G, Lu T. *Rare Met Mater Eng* 2011;40(12):2076–9.
- [22] Raftenberg MN, Mock Jr W, Kirby GC. *Int J Impact Eng* 2008;35(12):1735–44.
- [23] Kim Youngman, Lee Jae-Chul. *Mater Sci Eng A* 2006;420:8–12.
- [24] Sharma Rajneesh, Mahajan Puneet, Mittal Ramesh Kumar. *Carbon* 2012;50(8):2717–25.